2011

Design of Integrated Nanostructured Wicks for High-Performance Vapor Chambers

Justin A. Weibel
Purdue University

S V. Garimella
Purdue University, sureshg@purdue.edu

Jayathi Y. Murthy
Purdue University

David H. Altman
Raytheon

Weibel, Justin A.; Garimella, S V.; Murthy, Jayathi Y.; and Altman, David H., "Design of Integrated Nanostructured Wicks for High-Performance Vapor Chambers" (2011). *CTRC Research Publications.* Paper 155.
http://dx.doi.org/10.1109/TCPMT.2011.2132721

Design of Integrated Nanostructured Wicks for High-Performance Vapor Chambers

Justin A. Weibel, Suresh V. Garimella, Jayathi Y. Murthy, and David H. Altman

***Abstract*—The performance of passive phase-change cooling devices, such as vapor chambers or heat pipes, may be significantly enhanced by exploiting the superior thermal properties of carbon nanotube (CNT) arrays. The potential for large reductions in overall package resistance with the use of high-conductivity wick materials enhanced with CNT nanostructures is investigated. While such nanostructured wicks feature very small pore sizes which support high capillary pressures, it is shown that the high fluid flow resistance through these dense arrays prevents their use as the lone fluid transport mechanism. It is proposed that evaporator surfaces composed of nanostructured wicks fed by interspersed conventional wick materials (such as sintered powders) can provide the required permeability for fluid flow while simultaneously decreasing the effective evaporator thermal resistance. Optimization of wicks with integrated sintered and nanostructured areas requires a study of the trade-offs between the greater permeability of the sintered materials and the greater capillary pressure and thin-film evaporation area offered by the nanostructures. A numerical model is developed to estimate the thermal resistance of the evaporator region compared to that of a homogeneous sintered powder wick. The inputs needed for this model include the permeability and capillary pressure in the two regions. A parametric study is conducted as a function of the ratio of conduction and evaporative resistances for the nanostructured and sintered regions. For a given heat input, the optimal liquid-feeding geometry that minimizes thermal resistance is obtained. In the best cases, the thermal resistance is reduced by a factor of thirteen through the use of the integrated nanostructured wicks compared to the resistance of a homogeneous sintered powder wick.**

***Index Terms*—Evaporation, heat pipe, vapor chamber, thermal resistance, wick, carbon nanotube (CNT)**

NOMENCLATURE

A	Area (m^2).
d	Diameter (m).
h	Wick layer thickness (m).

Manuscript received June 25, 2010. This material is based upon work supported by the Defense Advanced Research Projects Agency (DARPA) and Space and Naval Warfare Systems Center (SPAWAR/SYSCEN) San Diego, CA under Contract No. N66001-08-C-2011.

J. A. Weibel, S. V. Garimella, and J. Y. Murthy are with the School of Mechanical Engineering and Birck Nanotechnology Center, Purdue University, West Lafayette, IN 47907 USA (Corresponding author e-mail: sureshg@purdue.edu).

D. H. Altman is with Raytheon Integrated Defense Systems, Sudbury, MA 01776 USA.

h_{fg} Latent heat of vaporization (J/kg).

k Thermal conductivity (W/mK).

k_{eff} Porous media effective conductivity (W/mK).

$\dot{m}$ Mass flow rate (kg/s).

$\dot{m}_{total}$ Total mass flow rate (kg/s).

ΔP Pressure drop (N/m^2).

P_{cap} Capillary pressure (N/m^2).

P_{drop} Pressure drop in wick (N/m^2).

p Pitch (m).

q Heat input (W).

R Thermal resistance (K/W).

r Radial distance (m).

r_p Pore radius (m).

r_{bulk} Bulk sintered powder area radius (m).

r_{evap} Evaporator area radius (m).T_{base}Uniform evaporator base temperature (K).

T_{vapor} Vapor temperature (K).

ΔT_{req} T_{base} - T_{vapor} (K).

z axial distance (m).

Greek symbols

ε Volumetric porosity.

θ Contact angle.

K Permeability (m^2).

μ Dynamic viscosity (Ns/m^2).

v Kinematic viscosity (m^2/s).

ρ Density (kg/m^3).

σ Surface tension (N/m).

υ R-component of velocity (m/s).

Φ Wedge geometry angle.

ω Z-component of velocity (m/s).

Subscripts

baseline	Baseline reference case.
CNT	CNT property.
cond	Conduction resistance.
cu	Copper property.
dryout	Capillary dryout parameter.
evap	Evaporation resistance.
l	Liquid property.
s	Sintered powder property.

Superscripts

*	Dimensionless quantity.
"	Surface area dependent quantitiy.

I. Introduction

Continued advances in the electronics packaging industry have led to components with greater power dissipation being integrated into ever-decreasing package sizes. This trend requires novel cooling solutions that provide for minimal overall thermal resistance between the component and the ambient to ensure reliable, low-temperature operation. Heat pipes and vapor chambers are widely used as thermal management devices for high-flux cooling applications. These devices are particularly suitable for applications that demand passive operation in confined geometries where conventional air cooling solutions are insufficient or unfeasible. Vapor chambers enclose a porous wicking material and working fluid within a chamber with distinct heat input and condensing sections. Fluid is locally evaporated at the heat input section and is replenished by capillary wicking of fluid from the condenser. By taking advantage of the high evaporation and condensation effective heat transfer coefficients, the overall package thermal resistance can be considerably lower than a solid conduction heat spreader alternative. Integration of emerging nano-materials into vapor chambers by means of advanced micro-fabrication techniques provides one possible path for meeting increasingly challenging cooling demands.

Owing to the high axial conduction and small height relative to a conventional wick structure, use of a carbon nanotube (CNT) array can minimize the conduction resistance across the evaporator section. The small pore structure supported by the CNT array can also result in an increase in the area of the thin liquid film, leading to higher evaporative heat transfer rates. While there has been limited investigation into thin-film evaporation enhancement using CNT arrays, several studies have explored pool boiling from CNT-coated surfaces and observed improved thermal performance [1], [2]. Additionally, the porosity of a densely grown

array of CNTs generates significant capillary pressure. Zhou et al. [3] demonstrated the viability of using CNTs directly as a nano-wick material capable of transporting fluid through capillary action. Fig. 1 shows an axisymmetric cross section of a vapor chamber with the sintered powder material at the evaporator section replaced by a CNT array. Cai and Chen [4] also proposed using CNT arrays as wicking structures for high-flux cooling applications. The arrays in their study were patterned to form 50 μm wide CNT-free channels to provide low-flow-resistance paths. Such a CNT wick structure was able to maintain a surface at a 35-45 °C superheat for a heat flux of 600 Wcm^{-2} with water as the working fluid. The predicted thermal resistance of nanostructured evaporators can be further incorporated into higher level heat pipe models to predict overall device performance enhancement [5].

The goal of the current study is to assess the thermal resistance reduction provided by a CNT array fed by patterned sintered copper powder wicks. Numerical flow models are employed to calculate the pressure drop within the evaporator to predict when capillary dryout occurs. The approach is similar to the analytical model of Wang and Peterson [6] for estimating capillary evaporation limits in thin porous layers, except that more complex and bi-porous geometries can be evaluated using the approach developed here. The geometry can thus be parametrically altered to maximize the area of the low-thermal-resistance CNT area while maintaining appropriate fluid feeding through a bulk micro-wick material. The particular bulk wicking material considered in the model is a sintered copper powder, although the method is general and can be applied to any feeding structures. The working fluid considered is water.

II. Wicking Structures and Physical Properties

Two important fluid flow properties of wick materials for the purposes of determining capillary flow limitations are the pore radius and the permeability. The pore radius directly relates to the capillary pressure as

$$P_{cap} = \frac{2\sigma\cos(\theta)}{r_p}. \quad (1)$$

As the pores become smaller, a larger capillary pressure is generated to drive the flow. However, the permeability, a measure of the ease of flow through the wick, decreases with decreasing pore size. This unavoidable trade-off between capillary pressure and flow resistance determines the maximum working distance for a given fluid flow rate within the wick (or equivalently, for a given total evaporation rate). The present analysis considers a single geometry each for both the sintered powder and the CNT microstructure with particular values for pore radius and permeability. The focus is on varying the macroscopic evaporator geometry to minimize flow resistance.

The CNT array parameters are typical of nanotube growth by microwave plasma-enhanced chemical vapor deposition (PECVD) using a titanium-aluminum-iron trilayer catalyst on a copper substrate with 200 W microwave plasma at 10 torr for 10 minutes [7]. CNTs are naturally hydrophobic and require functionalization via metallization or an acid treatment process. The diameter and length of a single nanotube are taken as 50 nm and 20 μm, respectively, with an array density of $2\text{x}10^{9}$ CNTcm^{-2}. For the purposes of estimating the permeability and pore radius, the array is assumed to consist of square-packed vertical cylinders as shown in Fig. 2. For this packing arrangement the array density translates to a porosity of 0.90. The permeability of the CNT array is calculated to be $7.18\text{x}10^{-16}$ m^2 from the analytical solution for flow through square-packed vertical cylinders provided by Larson and Higdon [8]. The capillary pressure and pore radius (assuming a wetting fluid) are determined from the analysis of Ranjan *et al.* [9], who used the program, SURFACE EVOLVER [10], to calculate the static meniscus shape of fluid within the pore of square-packed vertical cylinders to predict the capillary pressure. Applying the model for a porosity of 0.90 yields a pore radius and capillary pressure of 200 nm and $7.2\text{x}10^{5}$ Pa, respectively.

The assumed bulk micro-wick material used in all models is composed of a sintered structure made from 50 μm particles yielding a porosity of 0.66. The thickness of the sintered porous layer is assumed to be 200 μm. A relatively small particle size is chosen in order to allow for the creation of fine geometry features. As will be seen later, this powder size does not limit the maximum flow, and the results of the study are relatively independent of the sintered copper powder flow properties. The permeability and pore radius are obtained from correlations for packed sintered spheres [11]. A permeability of $2.25\text{x}10^{-11}$ m^2 and a pore radius of 10.5 μm (P_{cap}= $1.37\text{x}10^{4}$ Pa) are obtained from the equations:

$$\mathrm{K}_s = \frac{d_s^2 \varepsilon^3}{150\left(1-\varepsilon\right)^2} \tag{2}$$

$$r_p = 0.21 d_s \tag{3}$$

A summary of the properties used in the analysis for the CNT array and sintered powder wick are presented in Table 1.

III. Model Development

This section presents the rationale and assumptions underlying the model developed to predict the thermal resistance enhancement provided by an integrated CNT array evaporator. In all cases, a circular evaporator section with a radius of 5 mm is assumed, and is representative of hot-spot thermal management. The fluid flow and pressure drop are solved for in the commercial software package, FLUENT [12], while heat transfer is accounted for by setting the mass flux at the surfaces undergoing evaporation. The heat transfer thus takes place via evaporation from a free surface fixed at the top of the porous layer. Also, it is assumed that there is no additional resistance to flow at the junction between the CNT and the sintered powder

regions. Several previous studies [13-15] support a continuum solution approach for liquid transport through a CNT array.

A. Pressure Drop in the CNT Array

While full coverage with CNTs over the 5 mm-diameter evaporator may seem beneficial for lowering the thermal resistance due to the high thermal conductivity of CNTs, the low permeability of the array also prevents fluid from being supplied to the entire surface, which can lead to a starved wick with poor performance. However, an analytical calculation of pressure drop through the CNT region first assumes the entire evaporator region to be covered with CNTs. Fig. 3 shows an axisymmetric view of this configuration. The continuity and r-momentum equations for steady, incompressible fluid flow in an isotropic porous structure may be written as

$$\frac{1}{r}\frac{\partial(r\upsilon)}{\partial r}+\frac{\partial(\omega)}{\partial z}=0 \tag{4}$$

$$\frac{1}{\varepsilon^2}\left(\upsilon\frac{\partial\upsilon}{\partial r}+\omega\frac{\partial\omega}{\partial z}\right)=-\frac{1}{\rho_l}\frac{\partial P}{\partial r}-\frac{\nu_l\upsilon}{K}+\frac{\nu_l}{\varepsilon}\left[\frac{1}{r}\frac{\partial}{\partial r}\left(r\frac{\partial\upsilon}{\partial r}\right)-\frac{\upsilon}{r^2}+\frac{\partial^2\upsilon}{\partial z^2}\right] \tag{5}$$

While the CNT array is not an isotropic structure, the radial permeability may be assumed constant and, if fully developed, one-dimensional, uniform flow in the radial direction is assumed, the r-momentum equation simplifies to

$$\frac{dP}{dr}=-\frac{\mu_l\dot{m}}{\rho_l A(r)}\left[\frac{1}{K}+\frac{1}{\varepsilon r^2}\right]. \tag{6}$$

Accounting for the decreasing mass flow rate in the r-direction due to uniform evaporation from the top surface

$$\dot{m}(r)=\dot{m}_{total}\frac{\pi r^2}{\pi r_{evap}^2}, \tag{7}$$

and integrating from the outer edge of the CNT region at r_{evap} to a radius r, the expression for the pressure drop over this annular region can be obtained as

$$\Delta P=\frac{\mu\dot{m}_{total}}{2\pi\rho h}\frac{1}{r_{evap}{}^2}\left[\frac{1}{2K}\left(r_{evap}{}^2-r^2\right)+\frac{1}{\varepsilon}\ln\left(\frac{r_{evap}}{r}\right)\right]. \tag{8}$$

For a relatively low heat input of 10 W, with an equivalent mass flow rate of

$$\dot{m}_{total}=\frac{q}{h_{fg}}, \tag{9}$$

it is found that the liquid pressure drop exceeds the capillary pressure generated within the first millimeter of flow distance. While the small pores of the CNT array provide orders of magnitude larger capillary pressure than conventional micro-wicks, the permeability of the array is too limiting even to support flow rates corresponding to moderate heat inputs. In order to exploit CNTs for wicking action as well as for adequate permeability, a novel feeding mechanism is required to reduce the pressure drop within the CNT region.

B. Nanostructured Geometry and Thermal Resistance Model

One approach to realizing the thermal benefits of a CNT array in spite of their low permeability is by interspersing a patterned micro-wick into the CNTs in the 5 mm radius evaporator region. While the micro-wick would increase the overall thermal resistance, it could ensure that the CNT array is fed with liquid by reducing both the required wicking distance through the CNT array and the inlet mass flux to the CNT regions. This trade-off between added fluid supply and the reduced CNT area due to the interspersed micro-wick motivates the present analysis to identify a geometry that could provide a net gain in performance.

The geometry selected for this integration is a series of alternating wedges of CNT and micro-wick layers of equal angles, Φ, covering the entire evaporator area. This geometry was chosen because it easily allowed the evaporator to be parametrically segmented into multiple sized CNT sections and is feasible to manufacture. Fig. 4(a) depicts a representative unit cell section of this geometry showing the wedges with CNTs and the micro-wick. This section of the wedge is modeled with symmetry boundary conditions on the cut sides. The radius of the bulk wick material, r_{bulk}, is set at 12.5 mm in the model. However, it was verified that the results are independent of this parameter because the total pressure drop in the sintered material up to the evaporator section is negligible compared to that in the CNT array. Fig. 4(b) illustrates the simplified evaporator thermal and fluid flow conditions that are modeled. Evaporation is assumed to occur from the top and vertical surfaces of both the CNTs and sintered powder only within the central evaporator region. The individual evaporation mass fluxes from wedges of each material are adjusted such that the total heat input is split amongst the number of wedges required to fill a full 360° evaporator region, allowing for direct comparison between different cases with the wedge angle varied. The mass flux required for a given heat input is split between the CNT and sintered powder sections based on the parallel resistances to heat flow of the two layers according to

$$\dot{m}''_{CNT} = \frac{\Delta T_{req}}{R''_{CNT} h_{fg}}; \dot{m}''_{S} = \frac{\Delta T_{req}}{R''_{S} h_{fg}} \tag{10}$$

where

$$\Delta T_{req} = T_{base} - T_{vapor} = \frac{q}{A_{CNT} / R''_{CNT} + A_{S} / R''_{S}} . \tag{11}$$

The entire base of the evaporator is assumed to be at a uniform temperature. This is a reasonable assumption as the separate wedge sections have a small angle and the high conductivity of the heat pipe wall smoothes out any temperature differences induced by dissimilarities in the heat transfer coefficients over the separate wedge regions. The mass flux of the sections is therefore only a function of the heat input and the relative ratio of the thermal resistances of the CNT array and sintered powder wedges. The porosity and permeability of the CNT array and sintered powder are assigned to the different regions and the governing equations for steady, incompressible flow within porous media are solved in FLUENT to obtain the pressure drop

throughout the structure. The fluid flow boundary conditions set according to the above formulations are captured in Fig. 4(c). A mesh independence study was performed to ensure that a mesh of 337,500 structured hexahedral finite volume cells provided a sufficiently-resolved solution independent of mesh size. At this mesh size, doubling the number of cells yields only a 0.25% change in the predicted maximum pressure drop.

Fig. 5 presents the pressure drop solutions for different wedge angles given a constant heat input and sintered powder to CNT array thermal resistance ratio. In order to readily draw comparisons between the performance of different evaporator geometries in terms of a single parameter, an expression for an overall, dimensionless evaporator thermal resistance is formulated based on the pressure drop results. For small wedge angles, the pressure drop never exceeds the capillary pressure in the CNT array or sintered powder regions. For this case the thermal resistance can be simply defined as

$$R = \frac{\Delta T_{req}}{q}. \tag{12}$$

For larger wedge angles, the pressure drop begins to exceed the available capillary pressure within the CNT array region. The area over which this occurs is considered to reach a dryout condition and no longer participates in heat transfer. This reduction of evaporative heat transfer from the wick is accounted for as an increased effective thermal resistance of the evaporator region according to

$$R = \frac{\Delta T_{req}}{\left(q - q_{dryout}\right)} \tag{13}$$

where

$$q_{dryout} = \dot{m}''_{CNT} A_{dryout} h_{fg}. \tag{14}$$

The calculated resistance values are then normalized against a baseline case which considers the evaporator region to consist entirely of sintered copper powder:

$$R^* = \frac{R}{R_{\text{baseline}}} \tag{15}$$

where

$$\Delta T_{\text{baseline}} = \frac{qR''_S}{\pi r_{evap}{}^2} \tag{16}$$

$$R_{\text{baseline}} = \frac{\Delta T_{\text{baseline}}}{q} \tag{17}$$

This formulation is particularly useful because it yields a measure of the effective reduction in evaporator thermal resistance provided by the proposed geometries compared to a conventional homogeneous sintered powder evaporator.

C. Parametric Studies

The dimensionless resistances are found for a set of test cases. Variation of the wedge angle, Φ, shows how this resistance varies as the evaporator is subdivided into smaller separate CNT array and sintered powder regions. This wedge angle variation is performed for a set of different heat inputs and sintered powder to CNT array thermal resistance ratios (R''_S/R''_{CNT}). The dependence of the results on the heat input provides insight into the change in evaporator design guidelines with changing heat load. A range of R''_S/R''_{CNT} ratios are selected for the analysis to account for large uncertainty in the enhancement potential of the CNT array.

The wedge angle is varied from 3° to 60°. Below this angle, the reduced sizes of the sintered powder features become impractical to fabricate from 50 μm particles. The range of R''_S/R''_{CNT} is predicted based on the relative conduction resistances of the two layers, since the two-phase evaporation resistance is significantly lower than the conduction resistance through the saturated wick. A wide range of sintered powder effective conductivities are cited in the literature. These values generally fall between the limits for the effective conductivity of porous materials predicted by the Effective Medium Theory (EMT) equation and the Maxwell-Eucken model [16]:

$$\text{EMT: } (1-\varepsilon_l)\frac{k_{cu}-k_{eff}}{k_{cu}+2k_{eff}}+\varepsilon_l\frac{k_l-k_{eff}}{k_l+2k_{eff}}=0 \qquad (18)$$

$$\text{Maxwell-Eucken: } k_{eff}=k_l\frac{2k_l+k_{cu}-2(k_l-k_{cu})(1-\varepsilon_l)}{2k_l+k_{cu}+(k_l-k_{cu})(1-\varepsilon_l)} \qquad (19)$$

For a copper sintered powder saturated with water, these equations predict an effective conductivity range of 13-100 $Wm^{-1}K^{-1}$, corresponding to an approximate sintered powder thermal resistance from $1.5x10^{-6}$-$1.5x10^{-5}$ m^2KW^{-1} for a 200 μm layer. Cola et al. [17] measured the thermal resistance of CNTs grown on copper substrates by PECVD using a photoacoustic characterization technique. The thermal resistance of the CNT array was found to be $1.0\pm0.5x10^{-6}$ m^2KW^{-1}. These cited values for the different wick materials suggest a range for R''_S/R''_{CNT} from 1 to 25. The heat input is varied from 10-50 W. Above 50 W, the maximum superheat value for the highest resistance test case is likely to induce boiling in the wick, invalidating some of the principal assumptions of the model.

IV. Results and Discussion

The variation in performance of the integrated nanostructured evaporator with changing wedge angle is first investigated for a given heat input and R''_S/R''_{CNT} ratio. Fig. 6 presents these performance results in the form of relative dryout area, A_{dryout}/A_{CNT}, and the dimensionless evaporator resistance, $R/R_{baseline}$.

The first step in calculating and understanding the thermal performance is to track the amount of dried out CNT area for

different wedge angles. Fig. 6(a) shows that there is initially no dried out CNT area ($A_{dryout}/A_{CNT}=0$) for the low wedge angles because the total pressure drop across the small wedge remains below the capillary pressure. As expected, with an increase in wedge angle, the distance the fluid must travel to the center of the CNT region and the associated pressure drop increases until it eventually exceeds the capillary pressure. This leads to increasing dryout area with increasing wedge angle. The correlation between dryout area and thermal performance is depicted in Fig. 6(b). It is noted that when the dimensionless resistance is less than 1, the evaporator resistance is lower than the baseline case of a homogeneous sintered powder layer. Two distinct regions are observed in the resistance variation with wedge angle. The first is observed for small angles for which the resistance is constant and minimized, corresponding to the conditions of zero dryout area. In this region, because flow in the CNT array has no capillary flow limitation, the resistance is simply a function of the relative areas and resistances of the CNT and sintered powder layers. Because the total areas of CNTs and sintered powder do not change as the angle is varied, the resistance is constant. So long as $R''_S/R''_{CNT} > 1$ (i.e., the CNT layer is more conductive than the powder), unimpeded flow to the CNT areas will lead to improved performance compared to the baseline case, as is true in this case. The largest angle for which this minimum resistance occurs may be considered an optimal condition as further decreases in the feature size could result in greater manufacturing expense with no added performance benefits. This optimal angle occurs when the pressure drop in the CNT region is equivalent to the capillary pressure provided, just as the CNT area begins to be starved of liquid. For the conditions shown in Fig. 6, this optimal angle is approximately 10°. The second region of the graph begins just beyond the optimal angle. As the angle increases, larger portions of the CNT area become dried out, which eliminates their contribution to heat transfer and increases the evaporator thermal resistance. However, for a range of angles above the optimum value, there is still enough actively evaporating, low-resistance CNT array area to maintain the evaporator resistance below the baseline case. At some critical angle, however, the amount of dried-out CNT area is large enough that the resistance becomes larger than the baseline case.

The relative dryout area and dimensionless resistance versus wedge angle are shown in Fig. 7(a) and Fig. 7(b), respectively, for different heat inputs and a constant R''_S/R''_{CNT} ratio. As the heat input is lowered, the angle at which dryout begins and the previously defined maximum allowable optimum angle both increase. This occurs because there is a lower mass flow rate (and therefore less pressure drop) through the CNT section and a wider wedge can be used before the capillary pressure limitation is reached. The minimum evaporator resistance at the optimal angle, however, remains unchanged since the R''_S/R''_{CNT} is constant. The critical angle ($R^* = 1$) similarly decreases with increasing heat input. This is, in part, attributable to the more rapid increase in dryout area observed for higher heat fluxes with increasing wedge angle. It is concluded that higher heat inputs to the evaporator require more finely dispersed CNT nano-wick sections to achieve similar performance. Even for a conservative estimate of the CNT evaporation enhancement, the evaporator resistance can be reduced by more than 50% using interspersed 15° wedges; this

performance improvement is not possible without interspersed micro-wick feeding structures.

Fig. 8(a) and Fig. 8(b) show the relative dryout area and dimensionless resistance as a function of wedge angle for different R''_S/R''_{CNT} ratios at a constant heat input. When $R''_S/R''_{CNT} = 1$ (i.e., when the CNT array provides no reduction in resistance), the resistance is equivalent to the baseline case as expected and only worsens once the capillary limitation is exceeded and the CNT area begins to dry out. Incorporation of CNTs would not be recommended for such conditions. A more relevant observation is that the minimum evaporator resistance decreases with increasing R''_S/R''_{CNT}. As the CNT area becomes more efficient at removing heat from the surface compared to the sintered powder region, the evaporator resistance should decrease as long as fluid flow is not limited by the pressure drop. The required minimum optimum angle decreases slightly with increasing R''_S/R''_{CNT}. This occurs because more fluid is diverted into the more effective CNT area which leads to larger dryout areas (A_{dryout}/A_{CNT}) for increased R''_S/R''_{CNT}. However, this change is negligible for the heat inputs investigated. In addition to the obvious conclusion that a lower-resistance CNT array lowers the overall resistance, it is observed that the range of operating angles beneath the critical value ($R^*=1$) is significantly extended. For very large ratios of R''_S/R''_{CNT} when a majority of the CNT area is dried out, the small remaining evaporating area is still able to reduce the overall evaporator resistance compared to the baseline case. For the most optimistic case where $R''_S/R''_{CNT} =25$, even at $\Phi = 60°$ the failure angle is not reached and the minimum evaporator resistance is lowered by an order of magnitude compared to the baseline case.

For all the cases investigated with different heat inputs and R''_S/R''_{CNT} ratios, a significant enhancement potential is seen for the proposed integrated wick geometries. However, multiple different macroscopic evaporator geometry permutations could be conceptualized which would allow for further enhancement. In all of the cases above, the geometry was fixed such that the sintered powder and CNT wedges were of equal area. However, it was observed that the pressure drop in the sintered powder wedges was negligible, essentially rendering them to be fluid conduits of larger size than necessary, which act as thermal insulators relative to the CNTs. Taking advantage of this observation, a second evaporator geometry with sintered powder wedges that were half the size of the CNT wedges was evaluated. In theory, this would increase the low resistance CNT area without any negative performance impact so long as the pressure drop in the sintered powder wedges remained negligible. An assessment of this hypothesis is performed by comparing the thermal resistance of the proposed 2:1 A_{CNT} to A_S ratio geometry against the 1:1 ratio geometry for q = 20 W and $R''_S/R''_{CNT} = 5$, as shown in Fig. 9. As expected, the thermal resistance is reduced by 20% across all wedges angles due to the increased CNT area available for evaporation. Similar considerations could be used to arrive at additional evaporator geometries to further optimize overall performance versus manufacturing challenges.

V. Summary and Conclusions

The superior thermal and physical properties of carbon nanotubes justify investigation of their use as possible nano-wicking

structures in heat pipes to reduce the evaporative resistance. A numerical capillary limitation fluid flow model was developed to assess this potential reduction in evaporation thermal resistance. While a feeder wick pattern consisting of alternating wedges is selected for the analysis, the approach used and the conclusions drawn are applicable to general feeder wick arrangements. The key insights obtained from a parametric study using the model are:

1) The low permeability of CNT arrays prevents their use as a wicking material over a large area due to limitations on transport of working fluid.
2) Relatively high permeability micro-wicks can be interspersed throughout CNT arrays as fluid feeding structures to limit excessive pressure drop.
3) Using interspersed nanostructured wicking surfaces, the evaporator thermal resistance may be reduced significantly when adequately sized feeder wicks are utilized and the relative micro-wick to nano-wick area is optimized.
4) Given a feeder wick geometry, wick structure, and thermal requirements, there exists an optimal feature size that minimizes the evaporator resistance for the least micro-fabrication expense.

REFERENCES

[1] S. Ujereh, T. Fisher, and I. Mudawar, "Effects of Carbon Nanotube Arrays on Nucleate Pool Boiling," *International Journal of Heat and Mass Transfer*, vol. 50, pp. 4023-4038, 2006.

[2] H. S. Ahn, N. Sinha, M. Zhang, D. Banerjee, S. Fang, and R.H. Baughman, "Pool Boiling Experiments on Multiwalled Carbon Nanotube (MWCNT) Forests," *Journal of Heat Transfer*, vol. 128, pp. 1335-1342, 2006.

[3] J. J. Zhou, F. Noca, and M. Gharib, "Flow Conveying and Diagnosis with Carbon Nanotube Arrays," *Nanotechnology*, vol. 17, pp. 4845-4853, 2006.

[4] Q. Cai, and C-L. Chen, "Design and Test of Carbon Nanotube Biwick Structure for High-Heat-Flux Phase Change Heat Transfer," *Journal of Heat Transfer*, vol. 132, 052403, 2010.

[5] U. Vadakkan, S. V. Garimella, and J.Y. Murthy, "Transport in Flat Heat Pipes at High Heat Fluxes from Multiple Discrete Sources," *Journal of Heat Transfer*, vol. 126, pp. 347-54, 2004.

[6] Y. X. Wang and G. P. Peterson, "Analytical Model for Capillary Evaporation Limitation in Thin Porous Layers," *Journal of Thermophysics and Heat Transfer*, vol. 17, pp. 145-149, 2003.

[7] B. A. Cola, X. Xu, and T. S. Fisher, "Increased Real Contact in Thermal Interfaces: A Carbon Nanotube/foil Material," *Applied Physical Letters*, vol. 90, 093513, 2007.

[8] R. E. Larson and J. J. L. Higdon, "Microscopic Flow Near the Surface of Two-Dimensional Porous Media. Part 2. Transverse Flow," *Journal of Fluid Mechanics*, vol. 178, pp. 119-136, 1987.

[9] R. Ranjan, J. Y. Murthy, and S. V. Garimella, "Analysis of the Wick and Thin-Film Evaporation Characteristics of Microstructures," *Journal of Heat Transfer*, vol. 131, 101001, 2009.

[10] K. A. Brakke, "The Surface Evolver," *Experimental Mathematics*, vol. 1, pp. 141-165, 1992.

[11] A. Faghri, 1995, *Heat Pipe Science and Technology*, Taylor & Francis, Washington DC.

[12] Fluent Inc., 2004, FLUENT 6.2 User's Guide.

[13] B. M. Kim, S. Sinha and H. H. Bau, "Optical Microscope Study of Liquid Transport in Carbon Nanotubes," *Nanoletters*, vol. 4(11), pp. 2203-2208, 2004.

[14] J. H. Walther, T. Werder, R. L. Jaffe and P. Koumoutsakos, "Hydrodynamic Properties of Carbon Nanotubes," *Physical Review E*, vol. 69, pp. 062201, 2004.

[15] C. Fradin, A. Braslau, D. Luzet, D. Smilgies, M. Alba, N. Boudet, K. Mecke and J. Daillant, "Reduction in the Surface Energy of Liquid Interfaces at Short Length Scales," *Nature*, vol. 403, pp. 871-874, 2000.

[16] J. K. Carson, S. J. Lovatt, D. J. Tanner, and A. C. Cleland, "Thermal Conductivity Bounds for Isotropic, Porous Materials," *International Journal of Heat and Mass Transfer*, vol. 48, pp. 2150-8, 2005.

[17] B. A. Cola, J. Xu, C. Cheng, X. Xu, T. S. Fisher, and H. Hu, "Photoacoustic Characterization of Carbon Nanotube Array Thermal Interfaces," *Journal of Applied Physics*, vol. 105, 54313, 2007.

Justin A. Weibel received the B.S.M.E degree from Purdue University, West Lafayette, IN, in 2007.

He is currently pursuing his Ph.D. in Mechanical Engineering at Purdue University under the advisement of Suresh V. Garimella. His research involves experimental and numerical investigation of heat pipe operation and the optimization of capillary wicking structures.

Mr. Weibel was the recipient of the Helen and John Lozar Endowment Assistantship (2007-2009) and the Ingersoll-Rand Fellowship (2010) for graduate studies in Mechanical Engineering at Purdue University.

Suresh V. Garimella is the R. Eugene and Susie E. Goodson Distinguished Professor of Mechanical Engineering at Purdue University. He received his PhD from the University of California at Berkeley in 1989. He is Director of the NSF Cooling Technologies Research Center. His research interests include thermal microsystems, energy efficiency in computing and electronics, micro- and nano-scale transport phenomena, electromechanical microfluidic actuation, high-performance compact cooling technologies, renewable and sustainable energy systems, and materials processing. Dr. Garimella has co-authored over 350 refereed journal and conference publications and 13 patents/patent applications, besides editing or contributing to a number of books.

Dr. Garimella serves as Associate Editor of /ASME Thermal Science and Engineering/, and as an Editor of Applied Energy, International Journal of Micro and Nanoscale Transport and Experimental Heat Transfer, and has served as Associate Editor of ASME Journal of Heat Transfer and Editor of Heat Transfer-

Recent Contents and on the Editorial Board of Experimental Thermal and Fluid Science. He is a Fellow of the ASME. His efforts in research and engineering education have been recognized with the 2009 ASME Allan Kraus Thermal Management Award; 2010 Distinguished Alumnus Award from IIT Madras; 2009 Harvey Rosten Award for Excellence; 2004 ASME Gustus L. Larson Memorial Award; K16 Clock Award from the ASME; 2009 Purdue University Distance Teaching Award; Graduate School/UWM Foundation Research Award in recognition of Outstanding Research and Creative Activity, 1995; UWM Distinguished Teaching Award in recognition of Demonstrated Dedication to Excellence in Undergraduate Instruction, 1997; and Society of Automotive Engineers' Ralph R. Teetor Educational Award, 1992. Most recently, he was selected as a Jefferson Science Fellow (2010-'11)to provide scientific input to foreign policy issues in the U.S. State Department.

Jayathi Y. Murthy is Robert V. Adams Professor of Mechanical Engineering at Purdue University and Director of PRISM: NNSA Center for Prediction of Reliability, Integrity and Survivability of Microsystems,. She received her Ph.D degree from the University of Minnesota in the area of numerical heat transfer and has worked in both academia and in industry. During her employment at Fluent Inc., a leading vendor of CFD software, she developed the unstructured solution-adaptive finite volume methods underlying their flagship software Fluent, and the electronics cooling software package ICEPAK. More recently, her research has addressed sub-micron thermal transport, and the development of numerical techniques for concurrent electro-thermal simulation in emerging electronic devices. She is the recipient of the IBM Faculty Partnership award 2003-2005, the 2004 Journal of Electronics Packaging Best Paper award, the 2007 ASABE Best Paper Award, the 2008 ASME HTD Best Paper Award and the 2009 EPPD Woman Engineer of the Year award Prof. Murthy serves on the editorial board of *Numerical Heat Transfer*, is an editor of the 2nd edition of the *Handbook of Numerical Heat Transfer*, and serves as Associate Editor of the ASME *Journal of Heat Transfer*. She has served on numerous national committees and panels on electronics thermal management and CFD, and is the author of over 200 technical publications.

David H. Altman is a Principal Engineer in Raytheon Integrated Defense Systems Advanced Technology Programs Directorate. His work focuses on research and development into thermal management and energy system technologies for next generation defense electronics. His interests include development of advanced device scale, heat spreader, thermal interface, cold plate and cooling system technology incorporating emergent materials and system concepts. David holds BS and MS degrees from Rensselaer Polytechnic Institute and Boston University.

TABLES AND FIGURES

TABLE I

CNT ARRAY AND SINTERED POWDER PROPERTIES

Property	CNT	Sintered Powder
ε	0.90	0.66
r_p (μm)	$2.0x10^{-1}$	10.5
K (m^2)	$7.18x10^{-16}$	$2.25x10^{-11}$
h (μm)	20	200
R"$_{cond}$ (m^2K/W)	$0.5x10^{-6}$ - $1.5x10^{-6}$	$1.5x10^{-6}$ - $1.5x10^{-5}$
Φ	3-60°	

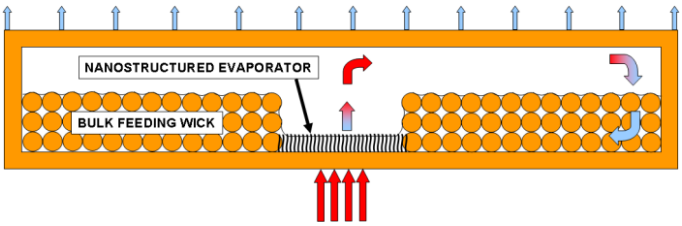

Fig. 1. Schematic illustration of a vapor chamber with an integrated nanostructured wicking material in the evaporator section.

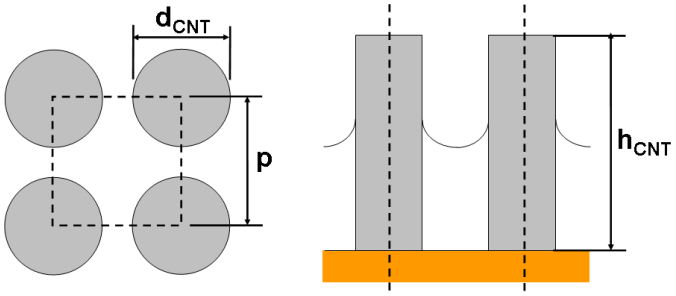

Fig. 2. CNT geometry approximated as an array of square-packed vertical cylinders: d_{CNT} = 50 nm, h_{CNT} = 20 μm, p = 268 nm (corresponds to ε = 0.90).

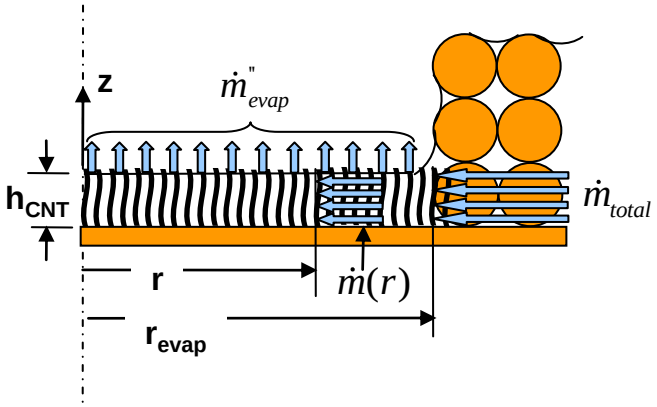

Fig. 3. Axisymmetric cross section depicting the steady radial flow through a CNT array fed at a radius r_{evap}.

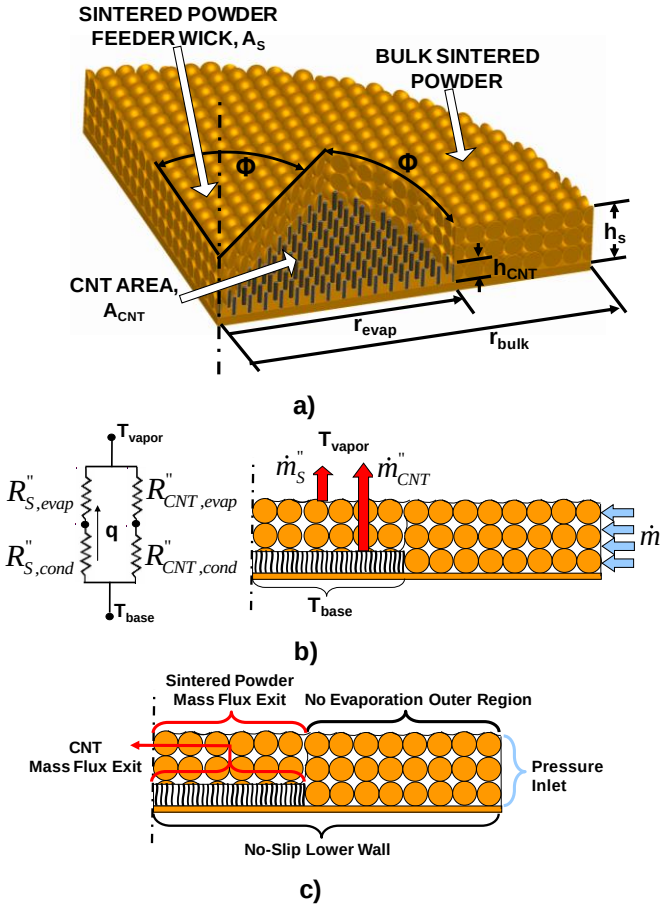

Fig. 4. (a) Schematic diagram of the 3-D wedge geometry chosen for the integrated micro and nano-wick materials, (b) the schematic fluid flow paths, evaporator temperatures, and thermal resistance network that describes the modeled conditions, and (c) the actual fluid flow boundary conditions imposed.

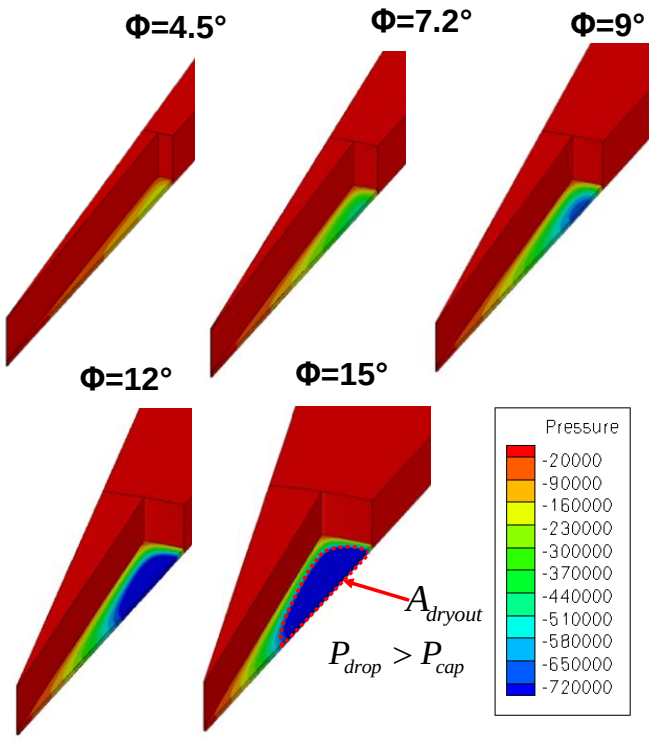

Fig. 5. Results for pressure drop (in Pa) with respect to a zero pressure inlet condition for varying wedge angles (q = 20 W, R''_S/R''_{CNT} = 5). The capillary pressure in the CNT region is 7.2×10^5 Pa and therefore, the dark blue region indicates the region where the pressure drop has been exceeded and dryout occurs.

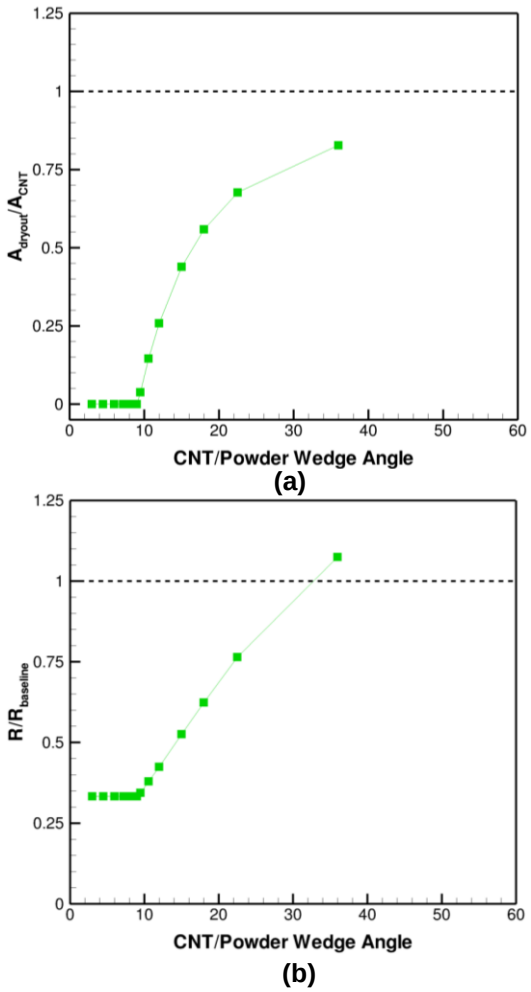

Fig. 6. Results from the parametric investigation of varying wedge angle, Φ. (a) The dryout CNT area per total CNT area, and (b) the dimensionless evaporator resistance are shown for a specific case of q = 20 W and $R''_S/R''_{CNT} = 5$. The dashed line represents a completely dried out CNT area in plot (a) and the baseline resistance case for a homogeneous sintered powder evaporator in plot (b).

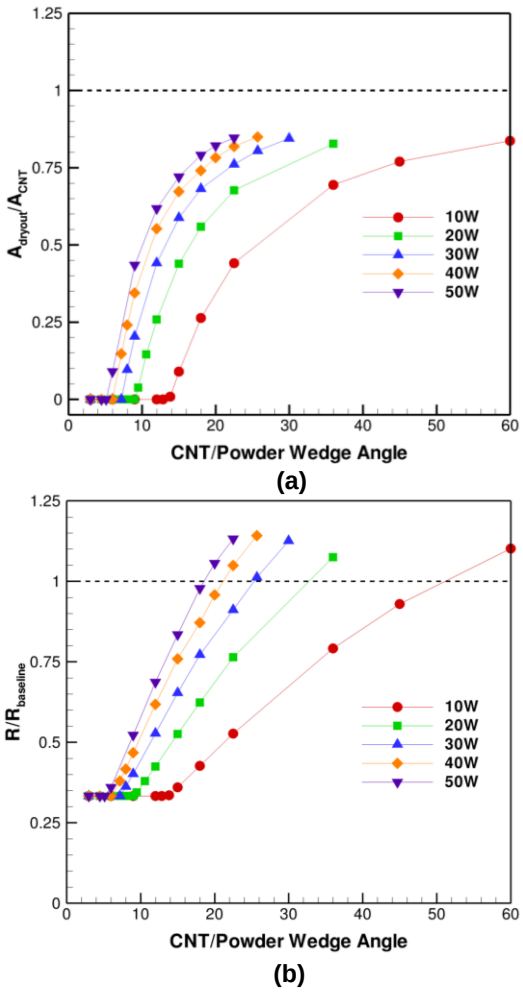

Fig. 7. Parametric investigation of varying heat inputs from 10-50 W for R''_S/R''_{CNT} = 5 showing (a) the dryout CNT area per total CNT area, and (b) the dimensionless evaporator resistance plotted as a function of the wedge angle, Φ.

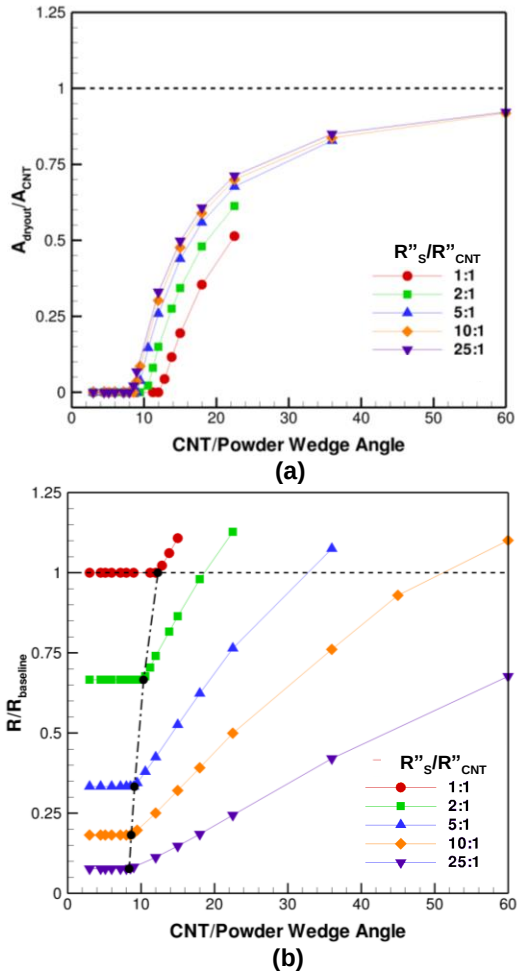

Fig. 8. Parametric investigation of changing R''_S/R''_{CNT} from 1-25 at q = 20 W, showing (a) the dryout CNT area per total CNT area, and (b) the dimensionless evaporator resistance plotted as a function of the wedge angle, Φ.

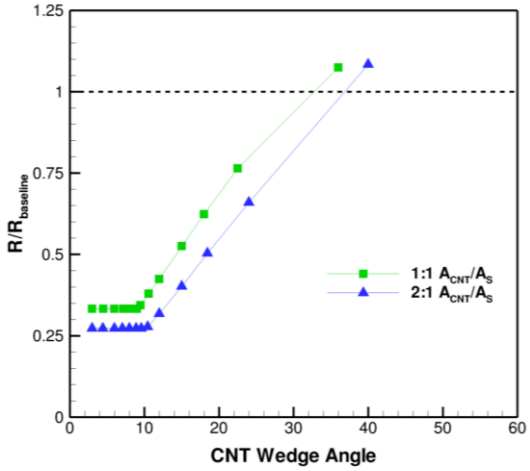

Fig. 9. Plot comparing two evaporator wedge patterns, differentiated by the relative size of their CNT versus sintered powder wedges. Comparison performed for q = 20 W and R''_S/R''_{CNT} = 5.